

Imaging Through Noise With Quantum Illumination

T. Gregory, P.-A. Moreau, E. Toninelli, and M.J. Padgett*

School of Physics and Astronomy, University of Glasgow,
Glasgow, G12 8QQ, UK

*To whom correspondence should be addressed; E-mail: miles.padgett@glasgow.ac.uk.

The contrast of an image can be degraded by the presence of background light and sensor noise. To overcome this degradation, quantum illumination protocols have been theorized that exploit the spatial correlations between photon-pairs. Here, we demonstrate the first full-field imaging system using quantum illumination, by an enhanced detection protocol. With our current technology, we achieve a rejection of background and stray light of up to 5.8 and also report an image contrast improvement up to a factor of 11, which is resilient to both environmental noise and transmission losses. The quantum illumination protocol differs from usual quantum schemes in that the advantage is maintained even in the presence of noise and loss. Our approach may enable laboratory-based quantum imaging to be applied to real-world applications where the suppression of background light and noise is important, such as imaging under low -photon flux and quantum LIDAR.

Introduction

Conventional illumination uses a spatially and temporally random sequence of photons to illuminate an object, whereas quantum illumination can use spatial correlations between pairs of photons to achieve performance enhancements in the presence of noise and/or losses. This enhancement is made possible by using detection techniques that preferentially select photon-pair events over isolated background events. The quantum illumination (QI) protocol was introduced by Lloyd [1], and generalized to Gaussian states by Tan et al. [2], where they proposed a practical version of the protocol. Quantum illumination has applications in the context of quantum information protocol such as secure communication [3, 4] where it secures communication against passive eavesdropping techniques that take advantage of noise and losses. The protocol has also been proposed to be useful for detecting the presence of a target object embedded within a noisy background, despite environmental perturbations and losses destroying the initial entanglement [5, 6, 7].

In 2013, Lopaeva et al. performed an experimental demonstration of the quantum illumination principle, to determine the presence or absence of a semi-transparent object, by exploiting intensity correlations of

a quantum origin in the presence of thermal light [8]. Additionally, a quantum illumination protocol has been experimentally demonstrated in the microwave domain [9] and a further demonstration in which joint detection of the signal and idler is not required [10]. However, these previous demonstrations were restricted to simply detecting the presence or absence of a target, rather than performing any form of spatially resolved imaging. The acquisition of an image using quantum illumination has recently been reported [11], but that demonstration was performed using a single-transverse-mode source of correlated photon pairs and by raster-scanning the object within one of these single-mode beams. The aforementioned demonstration may be seen as a qualitative assessment of the method but a full field imaging implementation of the quantum illumination protocol remains to be demonstrated using a multi-transverse-mode source of single photons and spatially resolved coincidence detections. Furthermore, the work in [11] uses only a coherent state as the incoming background light rather than a thermal state as was used in [8]. The use of thermal light as the incoming background light, as does the work presented here, better represents environmental light statistics and therefore performing full-field imaging using quantum illumination would be a demonstration of the potential real-world applications of the quantum illumination protocol.

In quantum imaging, commonly used properties are spatial quantum-correlations, which can be exploited to surpass the classical limits of imaging [12, 13, 14, 15, 16]. These quantum-correlations have been used in the case of NOON states for enhanced phase detection [17, 18], through the use of definite number of photons, to improve the signal to noise ratio for measuring the absorption of objects through sub-shot-noise measurements [15, 19, 20, 21], and to perform resolution-enhanced imaging by centroid estimation of photon-pairs [22]. Such schemes rely on the ability to detect and utilise quantum properties after the probed object, and are therefore sensitive to decoherence through the introduction of environmental noise and optical losses that lead to severe degradation of the quantum enhancement [23]. These schemes are therefore limited to low-noise and high-detection efficiency conditions, and to the sensing of objects presenting relatively low absorption. These limitations make such schemes difficult to implement in real-world conditions. However, the quantum illumination protocol, as described by Lloyd [1], is resilient to environmental noise and losses.

In this work we utilise spatial correlations between downconverted photon-pairs to demonstrate the first quantum illumination full-field imaging protocol. The spatial quantum correlations are manifested in the entangled photon-pairs produced via spontaneous parametric downconversion (SPDC). The twin beams produced via the SPDC process are directed to different regions of an Electron Multiplying CCD (EMCCD) array detector. EMCCD array detectors have previously been used to measure spatial correlations between photon-pairs [24, 25, 26]. By performing a pixel-by-pixel AND-operation between two regions of an array detector containing the SPDC beams, we preferentially select correlated photon-pair events and reject uncorrelated background light and sensor noise events. As a result of this preferential selection, the quantum illumination AND-image resulting from the sum of these AND-events produces a contrast advan-

tage relative to the classically acquired image, comprising the simple sum of the raw events. This relative contrast advantage and background rejection is achieved through the suppression of both background light and sensor noise. We also show that the advantage of the quantum illumination protocol over a classical imaging scheme is maintained in the presence of both noise and losses. The quantum advantage that we report is relative to the optimum classical measurement obtained via photon-counting and not obtained via any phase-sensitive measurement. This is in order to perform the demonstration using equivalent experimental conditions to acquire both the classical image and the quantum illumination AND-image in which an identical optical system, illumination source, illumination level, and noise, are used to collect data as it is acquired within the same acquisition. A phase-sensitive detection method [2, 5] would require a different optical setup for the classical acquisition in addition to phase stability, and it would prove impractical to perform imaging in real world scenarios.

This demonstration of a quantum illumination full-field imaging protocol is an important development in the application of quantum technologies within a real-world setting in which background light and sensor noise requires suppression. Applications of quantum illumination protocols such as quantum LIDAR will become more viable as multi-pixel SPAD arrays that are capable of time-tagging single-photon events are developed. As opposed to the EMCCD camera we use here, an Andor iXon Ultra 888 with a single-frame acquisition time of ~ 0.015 s for our acquisition parameters (see the materials and methods section for full details regarding camera acquisition parameters), the current generation of SPAD arrays being developed have increased acquisition speed and time resolution with frame rates of 100 kfps and gate times of 4 ns respectively being achievable [27]. An improvement of around seven orders of magnitude in the temporal resolution of the detector will potentially allowing useful depth measurements of a scene to be made.

Results

Imaging system. The experimental configuration is shown in Fig. 1. A 3 mm thick β -barium borate (BBO) non-linear crystal cut for type II degenerate downconversion is pumped by a collimated ~ 8 mm diameter laser beam at 355 nm to generate SPDC photon-pairs centred on the degenerate wavelength of 710 nm. A type-II phase-matched downconversion source results in the spatial separation of the two emitted SPDC beams labelled as the probe beam and the reference beam. The probe beam illuminates the object and may be subject to environmental losses and noise, while the reference beam neither interacts with the object nor is it subject to environmental losses and noise. After transmission through the crystal the pump beam is removed using a pair of dichroic mirrors and a pair of high-transmission interference filters mounted prior to the camera select the downconverted photon-pairs centred at the degenerate wavelength of 710nm. As shown in Fig. 1, the target object is placed in the far-field of the crystal such that the probe beam interacts with it while the reference beam has a free optical path. This plane is demagnified by a factor

of eight and imaged onto an EMCCD array detector, such that the two downconverted beams are imaged by different regions of the EMCCD array detector of pixel size $13 \times 13 \mu\text{m}^2$. The size of the correlations between the probe and reference beam in the far-field of the downconversion crystal depends upon the wavelength and diameter of the pump beam, and the effective focal length of the transform lens (L_1). For the configuration presented here this gives a correlation width of $\sigma \approx 4 \mu\text{m}$ in the plane of the EMCCD camera chip. A background light field is deliberately introduced using a thermal light source to illuminate a mask which overlays the probe beam through a reflection from a microscope slide slip cover (MS) placed in the image plane of the crystal. A thermal light source is used so as to simulate real-world conditions in which environmental noise will follow a similar distribution (i.e. noisier than a Poisson distribution) and be broad-band illumination. The level of demagnification for the quantum imaging arm was set to maximise the number of SPDC photon-pairs arriving in anti-correlated detector pixel positions while maintaining the ability to construct an image which is not under sampled. See the materials and methods section for full details regarding optical setup and camera acquisition parameters.

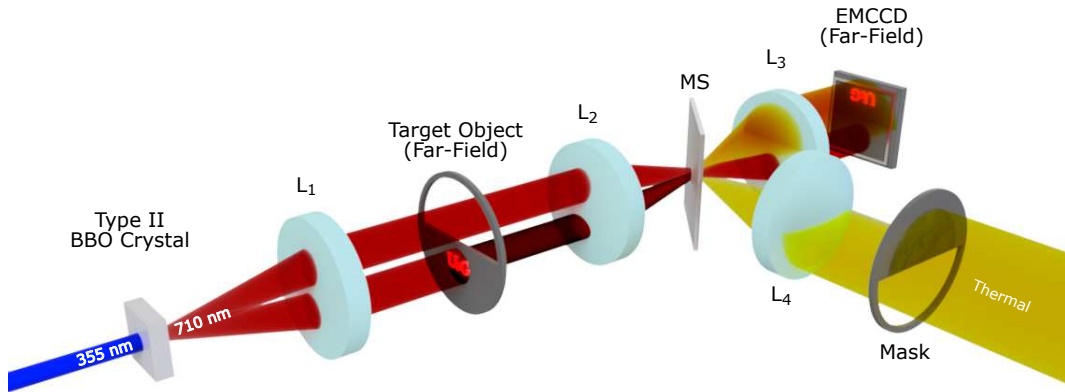


Figure 1: **Schematic of the quantum illumination experimental setup.** A BBO crystal cut for type-II downconversion is pumped by a UV laser to produce entangled photon-pairs via SPDC. The probe beam interacts with the Target Object placed in the far-field of the crystal while the reference beam has a free optical path. The lenses $L_1 = 75 \text{ mm}$, $L_2 = 400 \text{ mm}$, and $L_3 = 50 \text{ mm}$ comprise the quantum arm optics used to transform into the far-field, and then to demagnify by a factor of eight onto the EMCCD camera. A mask illuminated by thermal light is projected onto the camera using lenses $L_4 = 300 \text{ mm}$ and $L_3 = 50 \text{ mm}$ by reflection from the microscope slide slip cover (MS) placed in the image plane of the crystal.

We obtained our results using an illumination regime that was used by Tasca et al. (2013) [28] in which the threshold events per pixel per frame from the detection of SPDC photons matches the event rate due to the noise of the camera which for our detector and acquisition settings is ~ 0.0016 events per pixel per frame over the chosen acquisition region. As discussed above, background thermal illumination was added to the region of the sensor on which the probe beam is detected thereby simulating environmental noise at the probe beam wavelength which the quantum illumination protocol is able to reject. ND filters may be introduced after the target object to introduce optical losses as applied to the probe beam in order to

demonstrate the resilience to losses of the quantum illumination protocol.

Image analysis. To take advantage of the quantum illumination a simple pixel-by-pixel AND-operation between the two regions of the sensor that detect the reference and the probe beams within the same frame. This pixel-by-pixel AND-operation is equivalent to taking the Hadamard product of the two image arrays and is represented in Fig. 2 b) where it may be seen that those events that occur in diametrically opposite positions about the correlation peak are added together to build the quantum illumination AND-image. These events are selected by rotating the region of the camera frame corresponding to the probe beam through an angle of π to transform the momentum anticorrelation into a position correlation and then performing the AND-operation to select the pixel coordinates in which an event is detected in both the reference and the probe beam. Performing this operation serves to select the momentum-anticorrelated photon-pairs which comprise the correlation peak presented in Fig. 2 a). The result of this software AND-operation over a number of frames is then summed to build the AND-image. Performing this pixel-by-pixel AND-operation on correlated events, as opposed to the classically acquired image that constitutes single events and also includes both sensor noise events and background illumination, an advantage in contrast is achieved. This advantage is due to the fact that the AND-operation will preferentially keep the photon-pair events and will reject most of the uncorrelated events that arise from either sensor noise or unwanted background illumination.

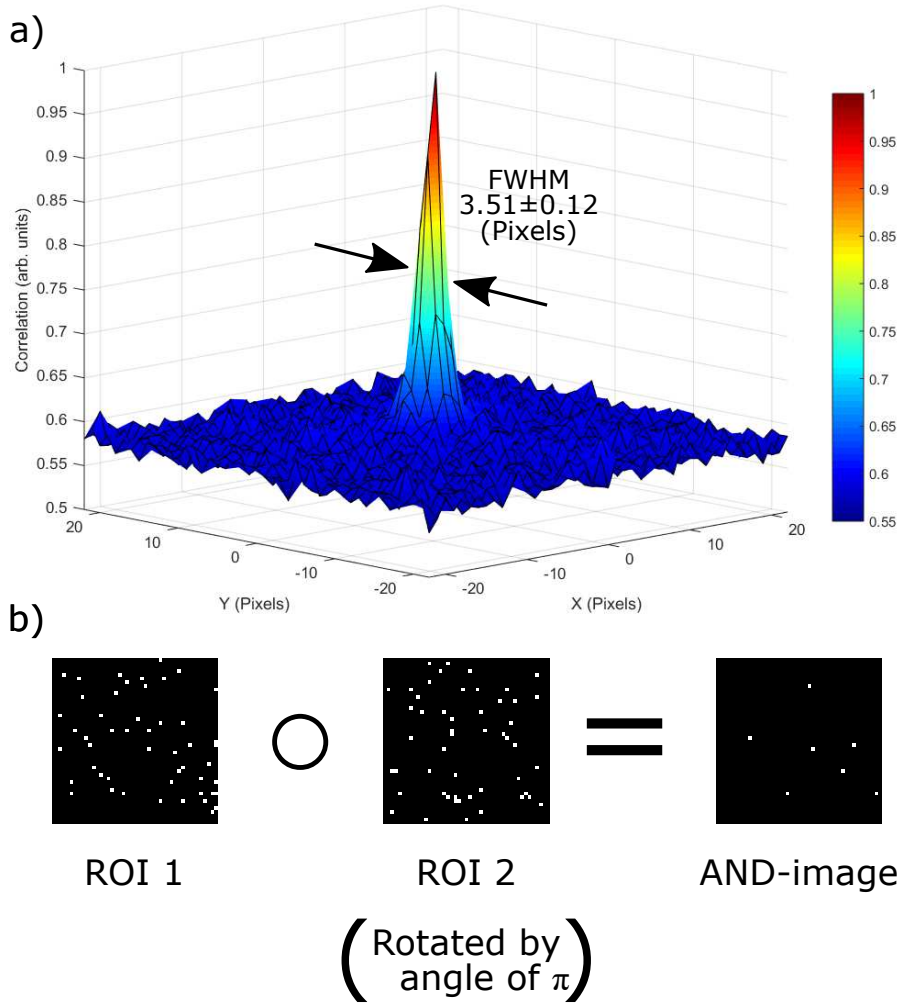


Figure 2: **Cross Correlation.** a) Correlation peak resulting from the cross-correlation of the two regions of interest that comprise the beams containing the photon-pairs. Calculated from 250,000 frames under an illumination regime identical to that in which the data was taken. b) Representation of the pixel-by-pixel AND-operation on a sum of 10 frames for visualisation purposes. Of the two regions of interest that comprise the regions of the frame on which the reference and probe beams are detected (ROIs) one must be rotated through an angle of π in order to transform the momentum anticorrelation into a position correlation such that the AND-operation selects the momentum anticorrelated photon-pairs.

The number of accidental coincidences between uncorrelated probe and reference events may be reduced by operating in a photon-sparse regime ($\ll 1$ events per pixel per frame). In addition, operating in such a low-light regime may be desirable due to requirements of non-intrusive detection. In the photon-sparse regime under which the system operates ($\ll 1$ events per pixel per frame after thresholding) the intensity correlations between classical beams are extremely weak [8] and therefore the comparison we use in this work is between the AND-image obtained using quantum illumination and the direct classical image. Both the AND-image and the classical image are acquired in the same acquisition using an identical optical setup. A general discussion on the optimal operating regimes for QI protocols can be found in [2] and in [8, 15] in the context of photon-counting strategies.

We show that the advantage of the quantum illumination protocol is that it is resilient to thermal background noise and to losses introduced into the probe arm. A theoretical description of the protocol can be found in the supplementary material. To perform a fair analysis of the results a distinction must be made between the background light and sensor noise, and the noise within the images that is due to shot-noise. The quantum illumination AND-images contain fewer events resulting from background light and sensor noise as evidenced by the removal of the cage in Fig. 3 but exhibit greater shot-noise \sqrt{n}/n , for which n is the number of events, when compared to the classically acquired image. The aim of our quantum illumination protocol is not to demonstrate an SNR improvement that would rely on sub-shot-noise statistics such as that demonstrated in Brida et al (2010) [19]. Rather, the aim of the quantum illumination protocol presented here is the rejection of background light and sensor noise which is achieved by the preferential rejection of uncorrelated events under the assumption of an unknown, potentially structured background. As discussed in [15], under the assumption that the background is known or can be independently estimated, the quantum illumination protocol will exhibit an advantage relative to the classically acquired image only when the number of accumulated photons per pixel is relatively low. In the case of an unknown background it is not possible to algorithmically subtract the background and as a result any subtraction applied may confuse or even deliberately mislead an interpretation of the true image.

Rejection of structured thermal illumination. The quantum illumination protocol works with arbitrary structured and a-priori unknown environmental background, which illustrates that the quantum illumination protocol works when a lack of knowledge of the background does not permit any ad-hoc background subtraction. We demonstrate that this quantum illumination protocol may be used to separate an object illuminated by the probe beam from a mask illuminated with thermal light. In Fig. 3 the bird and the fish are illuminated by the probe beam and the cage and net are illuminated by thermal light. By performing the same AND-analysis as previously described on the acquired frames to preferentially reject uncorrelated background light and sensor noise events the quantum-illuminated bird and fish may be distinguished from the thermally illuminated cage and net respectively.

In order to assess the distinguishability of the object we must consider both the image contrast and the signal to noise. For a final image comprising the quantum-illuminated target object, of average value, $\langle O \rangle$, above the dark regions of the image, and the thermally illuminated structured background, of average value, $\langle S \rangle$, above the dark regions of the image, the rejection of the structured illumination in the form of the cage or net may be characterised as background rejection, $R_{Q/C} = \langle O \rangle / \langle S \rangle$. The rejection ratio, RR , is taken to be the ratio of the values obtained from the quantum illumination AND-image, R_Q , and the classically acquired image, R_C , as per Equation 1.

$$RR = \frac{R_Q}{R_C} \quad (1)$$

While the above rejection ratio metric assesses the rejection of the thermal background illumination it

does not, however, take into account the shot-noise on the quantum-illuminated target object regions (σ_O). This noise (σ_O) will also affect the ability to distinguish the target object (O) from the thermally illuminated structured background (S). We therefore define a figure of merit, $D_{Q/C}$, to take into account the distinguishability of quantum-illuminated target object (O) against both the thermally illuminated structured background (S) and the noise on the object regions (σ_O) as per Equation 2.

$$D_{Q/C} = \frac{\langle O \rangle}{\langle S \rangle + \sigma_O} \quad (2)$$

Note that in the limit where a very large number of frames are acquired, and in the assumption that the noise σ_O is purely due to the shot noise, that is $\sigma_O = \sqrt{O}$, then the contribution of this noise in both D_C and D_Q vanishes. For the classically acquired image the limit in which this noise vanishes is under the acquisition of a smaller number of frames than for the quantum illumination AND-image due to a greater number of events being kept per frame. Under the limit of the acquisition of a very large number of frames the distinguishabilities become equivalent to the respective background rejection, R_C and R_Q , as defined previously. The maximum attainable image distinguishability advantage is therefore given by the reduction ratio, RR , and is achieved when a large number of frames are acquired, such that both the classical and quantum images are smooth.

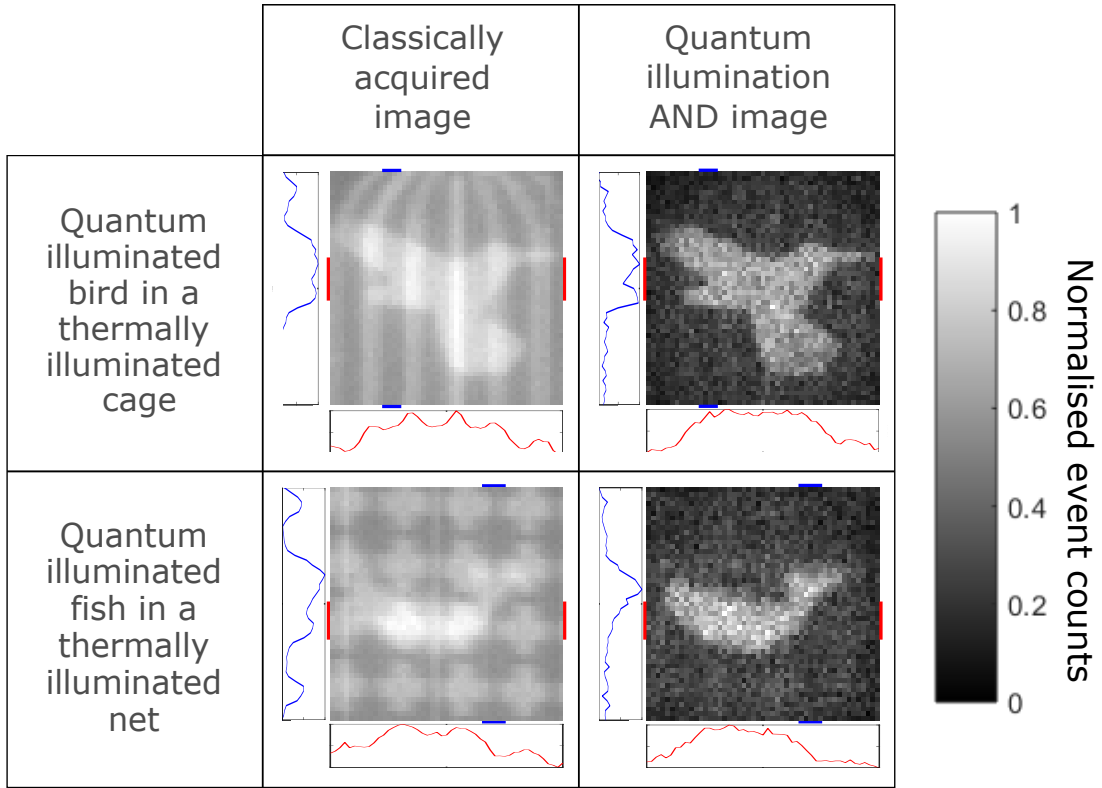


Figure 3: **Images of quantum illuminated target object preferentially selected over thermally illuminated mask.** Images of an object under quantum illumination overlaid with a thermally illuminated mask (second column). By applying the AND-operation on the data, the quantum illuminated object may be separated from the thermally illuminated mask (third column). In doing so the bird may be released from its cage and the fish released from its net. Red lines indicate the rows of the image used to generate the cut graph as shown below the images while blue lines indicate the columns used to generate the cut graph to the left of the images. Rows and columns used to generate the cut graphs as denoted by the red lines and blue lines respectively are rows 19-27 and columns 12-15 for the bird in a cage and rows 25-32 and columns 33-37 for the fish in a net. The scale of the cut graphs are normalised intensity (arbitrary units). Images are constructed over 2.5 million frames and are 49×49 pixels.

In Fig. 3 alongside the images horizontal and vertical cuts through the images are displayed in red and blue respectively. In the graphs referring to the classically acquired images there exist peaks corresponding to the thermally illuminated cage and net, while in the case of the graphs referring to the quantum illumination AND-images the prominence of these peaks are greatly reduced due to the preferential rejection of the uncorrelated background noise events. The graphs referring to the quantum illumination AND-image exhibit greater shot-noise due to the images containing fewer events than the classically acquired images and also some peaks remain identifiable in the cut graphs due to increased false correlations in local regions with an increased fill factor. For the bird in a cage as shown in Fig. 3 an improvement in the rejection ratio, RR, of a factor of order 4.2 is observed, and a value of 1.3 for the distinguishability metric D_Q/D_C , mainly limited here by the efficiency of our implementation.

Figure 4 displays the bird in a cage under a range of increasing levels of thermal illumination. In all cases

the prominence of the bars is reduced in the quantum illumination AND-image compared to the classically acquired image, however, some structure remains visible as a result of false correlations. The rejection of background and stray light for the images obtained under these illumination conditions as defined by the rejection ratio, RR , increases from 4.2 to 5.8 across as the level of thermal illumination increases. The distinguishability ratio D_Q/D_C which takes into account the variations within the quantum illuminated object is also shown to present an advantage in the case of the quantum illumination AND-image when compared to the classically acquired image. The distinguishability value may also be seen to increase with increasing thermal illumination of the cage and this is due to the quantum illumination AND-image not keeping all of the classical cage events and therefore D_Q will decrease at a slower rate than D_C for the classically acquired image.

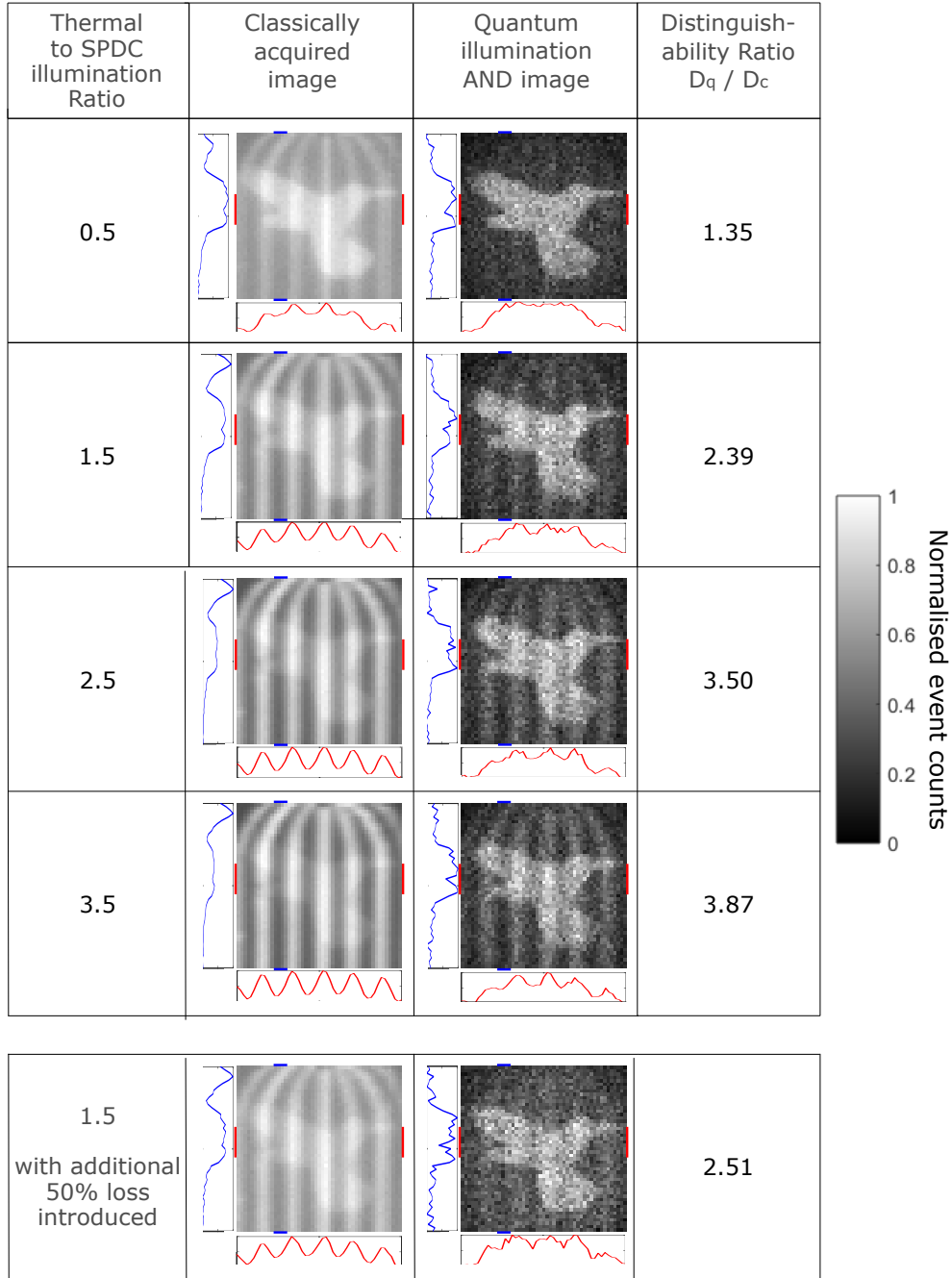


Figure 4: **Images of quantum illuminated target object preferentially selected over thermally illuminated mask with increasing thermal illumination and the introduction of losses.** Images of the bird under quantum illumination overlaid with a thermally illuminated cage (second column). By applying the AND-operation on the data, the quantum illuminated bird may be separated from the thermally illuminated cage (third column). In doing so the bird may be released from its cage. This is demonstrated across a range of increasing levels of thermal illumination represented in the first column as the ratio of the detected average intensity of the thermally illuminated cage image regions to the intensity of the quantum illuminated bird image regions. The final row presents results with the further introduction of $\sim 50\%$ optical losses into the probe beam by way of an ND filter. The distinguishability ratio D_Q/D_C is presented in the fourth column and increases with increasing thermal illumination of the cage. Red lines indicate the rows of the image used to generate the cut graph as shown below the images while blue lines indicate the columns used to generate the cut graph to the left of the images. Rows and columns used to generate the cut graphs as denoted by the red lines and blue lines respectively are rows 19-27 and columns 12-15 for the images. The scale of the cut graphs are normalised intensity (arbitrary units). Images are constructed over 2.5 million frames and are 49×49 pixels.

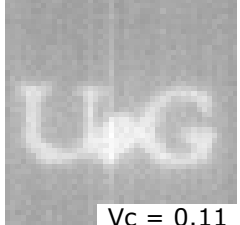
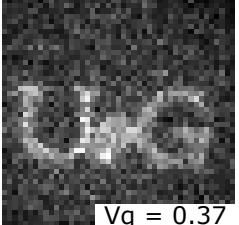
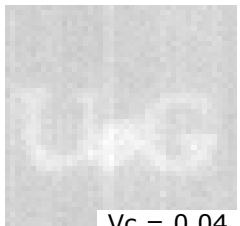
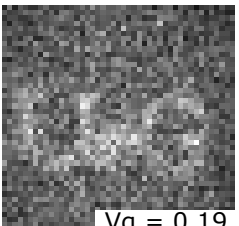
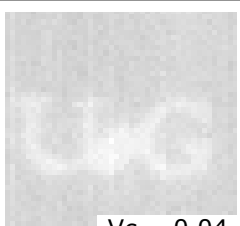
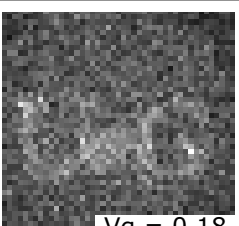
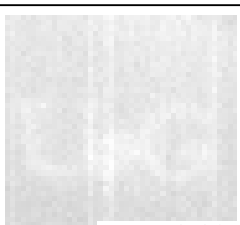
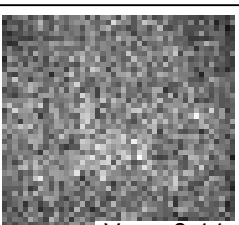
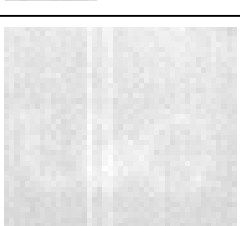
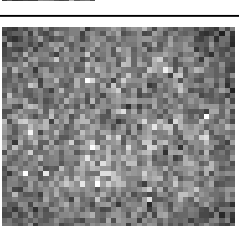
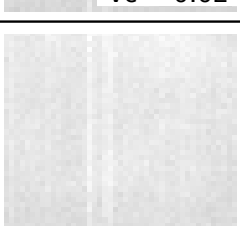
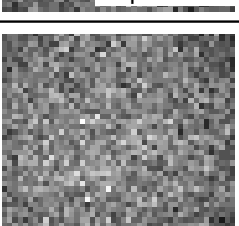
Quantum illumination advantage. Having demonstrated the use of the QI protocol in terms of rejection of background we now go on to assess the robustness of this quantum illumination protocol under differing loss and thermal noise levels and measure the ability of our QI scheme to reject the background thermal light and sensor noise. Here we apply an unstructured background so as to simplify the demonstration compared to a structured background as used above. We use the ratio between the contrasts of the quantum illumination AND-image and the classical image. In both cases, image contrast is quantitatively assessed using the Michelson contrast or visibility (V) as represented in Equation (3), in which the difference between the calculated intensities of the bright region (I_{max}) and the dark region (I_{min}) of the final summed image is divided by the sum of the intensities in the bright and dark regions.

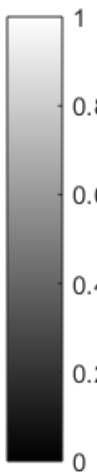
$$V_{Q/C} = \frac{I_{max} - I_{min}}{I_{max} + I_{min}} \quad (3)$$

To assess the advantage of the quantum illumination protocol, in this work we define the quantum illumination advantage, A , as the ratio between the contrast V_Q of the image acquired through quantum illumination (i.e. the image obtained by keeping only the correlated events through performing the AND-operation) and the contrast V_C of the image acquired simply by summing the probe-beam events over all frames.

$$A = \frac{V_Q}{V_C} \quad (4)$$

So as to verify that the scheme presented here is a quantum illumination scheme a binary mask of the University of Glasgow (UoG) initials laser cut from a piece of card was used as the target object. Figure 5 shows a comparison between performing the aforementioned AND-analysis on 1.5 million frames to the corresponding classical image over a range of increasing optical losses introduced into the probe arm of the system by means of a series of ND filters.

Transmission at 710nm (%)	Classically acquired image	Quantum illumination AND image	Quantum illumination advantage ratio $A = V_q/V_c$
100	 $V_c = 0.11$	 $V_q = 0.37$	3.36 ± 0.07
68.4	 $V_c = 0.04$	 $V_q = 0.19$	4.74 ± 0.17
54.8	 $V_c = 0.04$	 $V_q = 0.18$	4.57 ± 0.16
41.4	 $V_c = 0.02$	 $V_q = 0.11$	6.06 ± 0.41
34.2	 $V_c = 0.02$	 $V_q = 0.11$	6.64 ± 0.43
17.2	 $V_c = 0.006$	 $V_q = 0.06$	10.95 ± 1.30



Normalised event counts

Figure 5: **Imaging using quantum illumination with losses introduced.** Imaging using quantum illumination within a thermal background with optical losses introduced. Images of the UoG object with the classical image created by averaging all frames (second column), and the quantum illumination AND-image built from the sum of results of performing an AND-operation to select correlated events in the reference and probe beams (third column). The UoG object illuminated by the probe beam is imaged under the conditions of increasing optical losses (see the transmission of the ND filters placed into the probe beam at 710nm in the first column). The quantum illumination advantage A under these levels of optical losses for images constructed over 1.5 million frames is displayed in the fourth column. Images are 45×45 pixels.

From the images presented in Fig. 5 it is seen that the quantum illumination advantage, A , increases with the level of optical losses introduced. This increase in the quantum illumination advantage is due to the fact that the classical image contrast, in which all events are kept, degrades faster than that of the quantum illumination AND-image constructed using the result of the AND-operation (see supplementary material for a theoretical description of the effect). The quantum illumination advantage also increases with the level of background noise events introduced into the probe beam from a thermal source, as is the expected behaviour from the equations we present in the supplementary material. We also present the corresponding experimental results obtained under increasing levels of thermal illumination introduced into the system in the supplementary material.

In addition to the imaging results for this quantum illumination protocol we also consider how it may be used in an application where the presence or absence of an object needs to be assessed. This is the context in which Lloyd [1] originally proposed the quantum illumination protocol and has clear applications in realising quantum LIDAR or quantum RADAR applications. It can be demonstrated that a strategy combining the information from the classical data and the quantum data, both acquired through quantum illumination, will always lead to a bit-error-rate enhancement, as long as a contrast advantage is detected in the quantum data. This bit-error-rate enhancement in the context of quantum illumination protocols is discussed in the supplementary material.

Discussion

We have demonstrated a quantum illumination protocol to perform full-field imaging achieving a contrast enhancement through the suppression of both background light and sensor noise. Structure within the thermal background illumination is potentially a-priori unknown and therefore cannot be suppressed with a simple ad-hoc background subtraction. Through resilience to environmental noise and losses, such a quantum illumination protocol should find applications in real-world implementations including quantum microscopy for low light-level imaging, quantum LIDAR imaging applications, and quantum radar. Improvements in detector technologies such as SPAD arrays capable of time-tagging events should enable time-of-flight applications to be realised and applied outside of the laboratory through the increased acquisition speed and time resolution that they enable.

Materials and Methods

The source used for the pump is a JDSU xCyte CY-355-150 Nd:YAG laser with 355 nm output at 160 mW with pulse repetition 100 +/- 10 Mhz. The pump is attenuated to $\sim 1 \text{ mW mm}^{-2}$ and expanded to $\sim 8 \text{ mm}$ on the crystal via a spatial filter comprising a 50 mm lens, 25 μm pinhole, and a 200 mm lens. The downconversion source is a β -barium borate (BBO) non-linear crystal of dimensions $10 \times 10 \times 3 \text{ mm}$,

cut for type-II degenerate downconversion at 710 nm with a half-opening angle of 5° . The camera used here is an Andor iXon ULTRA 888 DU-888U3-CS0-#BV; of pixel size $13 \times 13 \mu\text{m}^2$, 100% fill-factor EMCCD camera. The camera was cooled to -90°C using liquid cooling. Optimal acquisition parameters for the camera were set as follows: vertical speed $1.33 \mu\text{s}$; voltage clock amplitude +0 V, horizontal speed 10 MHz; EM gain 1000; pre-amplifier gain set to 1; 128×128 pixel acquisition region; exposure time of 0.0149500 s (the shortest exposure time for given acquisition parameters).

The filters used in this experiment are Chroma T4551pxt dichroic mirrors (455 nm cut-off, 98% transmission at 710 nm) and Chroma ET710/10m interference filters (centred on the degenerate wavelength 710nm with a bandwidth of 10 nm and a top-hat profile, 99% transmission at 710 nm). Two interference filters are used as degenerate downconversion is not centered on the bandpass thereby resulting in unevenly sized downconversion beams. Further to placing one filter onto the camera the a second interference filter is orientated to shift its transmission profile and so select a narrower overall bandpass and more evenly sized beams.

To each of the frames acquired by the EMCCD camera a threshold is applied so as to minimise the camera readout noise events which dominates the low values of the Analog-Digital Converter (ADC) counts histogram for EMCCD cameras, while maximising the overall quantum efficiency of the system. A threshold of $T \approx \mu_{ro} + 3 \sigma_{ro}$ is appropriate in which μ_{ro} and σ_{ro} are the mean and standard deviation of the readout noise respectively. Any frames containing events of an extraordinary nature, taken to be those with pixel values of greater than 45,000, were removed from the dataset due their containing events caused by cosmic rays striking the detector. See also [21]. For the acquisition parameters used here a threshold of 510 is applied and this results in ~ 0.0016 camera noise events per pixel per frame.

References

- [1] S. Lloyd, Enhanced sensitivity of photodetection via quantum illumination. *Science* **321**, 1463–1465 (2008).
- [2] S.-H. Tan, B. I. Erkmen, V. Giovannetti, S. Guha, S. Lloyd, L. Maccone, S. Pirandola, J. H. Shapiro, Quantum Illumination with Gaussian States. *Physical Review Letters* **101**, 253601 (2008).
- [3] J. H. Shapiro, Defeating passive eavesdropping with quantum illumination. *Physical Review A* **80**, 022320 (2009).
- [4] Z. Zhang, M. Tengner, T. Zhong, F. N. C. Wong, J. H. Shapiro, Entanglement’s Benefit Survives an Entanglement-Breaking Channel. *Physical Review Letters* **111**, 010501 (2013).
- [5] S. Guha, B. I. Erkmen, Gaussian-state quantum-illumination receivers for target detection. *Physical Review A* **80**, 052310 (2009).

- [6] S. Pirandola, B. R. Bardhan, T. Gehring, C. Weedbrook, S. Lloyd, Advances in photonic quantum sensing. *Nature Photonics* **12**, 724–733 (2018).
- [7] M. Sanz, U. Las Heras, J. García-Ripoll, E. Solano, R. Di Candia, Quantum Estimation Methods for Quantum Illumination. *Physical Review Letters* **118**, 070803 (2017).
- [8] E. D. Lopaeva, I. R. Berchera, I. P. Degiovanni, S. Olivares, G. Brida, M. Genovese, Experimental realisation of quantum illumination. *Physical Review Letters* **110**, 153603 (2013).
- [9] S. Barzanjeh, S. Guha, C. Weedbrook, D. Vitali, J. H. Shapiro, S. Pirandola, Microwave quantum illumination. *Physical Review Letters* **114**, 080503 (2015).
- [10] C. W. Sandbo Chang, A. M. Vaddiraj, J. Bourassa, B. Balaji, C. M. Wilson, Quantum-enhanced noise radar. *Applied Physics Letters* **114**, 112601 (2019).
- [11] D. G. England, B. Balaji, B. J. Sussman, Quantum-enhanced standoff detection using correlated photon pairs. *Physical Review A* **99**, 023828 (2019).
- [12] M. Genovese, Real applications of quantum imaging. *Journal of Optics* **18**, 073002 (2016).
- [13] L. A. Lugiato, A. Gatti, E. Brambilla, Quantum imaging. *Journal of Optics B: Quantum and Semi-classical Optics* **4**, S176 (2002).
- [14] S. P. Walborn, C. H. Monken, S. Pádua, P. H. Souto Ribeiro, Spatial correlations in parametric down-conversion. *Physics Reports* **495**, 87–139 (2010).
- [15] A. Meda, E. Losero, N. Samantaray, F. Scafirimuto, S. Pradyumna, A. Avella, I. Ruo-Berchera, M. Genovese, Photon-number correlation for quantum enhanced imaging and sensing. *Journal of Optics* **19**, 094002 (2017).
- [16] P.-A. Moreau, E. Toninelli, T. Gregory, M. J. Padgett, Imaging with quantum states of light. *Nature Reviews Physics* **1**, 367–380 (2019).
- [17] V. Giovannetti, S. Lloyd, L. Maccone, Quantum-Enhanced Measurements: Beating the Standard Quantum Limit. *Science* **306**, 1330–1336 (2004).
- [18] T. Ono, R. Okamoto, S. Takeuchi, An entanglement-enhanced microscope. *Nature Communications* **4**, 2426 (2013).
- [19] G. Brida, M. Genovese, I. R. Berchera, Experimental realization of sub-shot-noise quantum imaging. *Nature Photonics* **4**, 227–230 (2010).
- [20] P.-A. Moreau, J. Sabines-Chesterking, R. Whittaker, S. K. Joshi, P. M. Birchall, A. McMillan, J. G. Rarity, J. C. F. Matthews, Demonstrating an absolute quantum advantage in direct absorption measurement. *Scientific Reports* **7**, 6256 (2017).

- [21] E. Toninelli, M. P. Edgar, P.-A. Moreau, G. M. Gibson, G. D. Hammond, M. J. Padgett, Sub-shot-noise shadow sensing with quantum correlations. *Optics Express* **25**, 21826 (2017).
- [22] E. Toninelli, P.-A. Moreau, T. Gregory, A. Mihalyi, M. P. Edgar, N. Radwell, M. J. Padgett, Resolution-enhanced quantum imaging by centroid estimation of biphotons. *Optica* **6**, 347-353 (2019).
- [23] V. Giovannetti, S. Lloyd, L. Maccone, Advances in quantum metrology. *Nature Photonics* **5**, 222–229 (2011).
- [24] P.-A. Moreau, J. Mougín-Sisini, F. Devaux, E. Lantz, Realisation of the purely spatial Einstein-Podolsky-Rosen paradox in full-field images of spontaneous parametric down-conversion. *Physical Review A* **86**, 010101 (2012).
- [25] M. P. Edgar, D. S. Tasca, F. Izdebski, R. E. Warburton, J. Leach, M. Agnew, G. S. Buller, R. W. Boyd, M. J. Padgett, Imaging high-dimensional spatial entanglement with a camera. *Nature Communications* **3**, 984 (2012).
- [26] H. Defienne, M. Reichert, J. W. Fleischer, General model of photon-pair detection with an image sensor. *Physical Review Letters* **120**, 203604 (2018).
- [27] I. Gyongy, N. Calder, A. Davies, N. A.W. Dutton, R. R. Duncan, C. Rickman, P. Dalgarno, R. K. Henderson, A 256×256 , 100-kfps, 61% fill-Factor SPAD image sensor for time-resolved microscopy applications. *IEEE Transactions on Electron Devices* **65**, 547-554 (2018).
- [28] D. S. Tasca, M. P. Edgar, F. Izdebski, G. S. Buller, M. J. Padgett, Optimizing the use of detector arrays for measuring intensity correlations of photon pairs. *Physical Review A* **88**, 013816 (2013).

Acknowledgements:

Funding: This work was funded by the UK EPSRC (QuantIC EP/M01326X/1) and the ERC (TWISTS, Grant no.340507). T.G. acknowledges the financial support from the EPSRC (EP/N509668/1) and the Professor Jim Gatheral Quantum Technology Studentship. P.A.M. acknowledges the support from the European Union Horizon 2020 research and innovation program under the Marie Skłodowska-Curie fellowship grant agreement No 706410, from the Leverhulme Trust through the Research Project Grant ECF-2018-634 and from the Lord Kelvin Adam Smith Leadership Fellowship Scheme. E.T. acknowledges the financial support from the EPSRC Centre for Doctoral Training in Intelligent Sensing and Measurement (EP/L016753/1).

Supplementary Text

Light Level

The regime in which is used as a baseline when no additional environmental losses or thermal light are introduced is the regime defined by Tasca et al. (2013) (28) in which the thresholded events per pixel per frame from the detection of SPDC events matches the thresholded event rate due to the clock induced charge of the camera. The clock induced charge of the camera using the aforementioned settings is ~ 0.0016 events per pixel per frame and therefore the event rate for the regions within the SPDC beams is set to be ~ 0.0032 events per pixel per frame. For this system the AND-efficiency, given as η below, has been estimated to be 0.0021056. This value is calculated to be the proportion of events that occur in the reference beam that have an anticorrelated event in the probe beam corrected for randomly correlated events. This value is determined from the data used to generate the correlation peak as displayed in Figure 3 in the main text. The quantum efficiency of the EMCCD camera (Andor iXon ULTRA 888 DU-888U3-CS0-#BV) is quoted as 77.75% when cooled to -100°C while we operate the camera at -90°C . However, as we describe above, we threshold each frame and this further reduces the detection efficiency as not all photons detected by the camera are registered as events in the thresholded frames.

Theory on contrast enhancement

We establish here an expression for the expected quantum illumination advantage as a function of experimental parameters. We show how the advantage depends on the losses in the target or probed arm, and as a function of the amount of thermal light. We note p_r the rate of SPDC photons detected in the reference arm, η is the apparatus arm efficiency i.e. including losses occurring in the quantum illumination arm at the exclusion of target losses such that the efficiency of the reference arm from the crystal to the camera included is $\eta_r = \eta$ and of the probe arm from the crystal to the camera included is $\eta_p = \eta\varepsilon$, where ε is the probe arm efficiency. This gives a detection rate of SPDC photons in the probe arm of $p_p = \varepsilon p_r$. We note d the dark count rates and T the thermal light rate. One can then write the AND event rate with the quantum correlated light as follows:

$$R_{Bright}^Q = \varepsilon\eta p_r + (p_r(1 - \varepsilon\eta) + d)(\varepsilon p_r(1 - \eta) + d + T) \quad (S1)$$

$$R_{Dark}^Q = (p_r + d)(d + T)$$

Where R_{Bright}^Q is the AND event rate detected in the bright part of the object and R_{Dark}^Q is the AND event rate detected in the dark parts of the object. One can as well express the rates in the classical simple average as follows:

$$R_{Bright}^C = \varepsilon p_r + T + d \quad (S2)$$

$$R_{Dark}^C = T + d$$

From these equations one can express the quantum illumination advantage A as a function of the experimental parameters by using:

$$A = \frac{(R_{Bright}^Q - R_{Dark}^Q)(R_{Bright}^C + R_{Dark}^C)}{(R_{Dark}^Q + R_{Bright}^Q)(R_{Bright}^C - R_{Dark}^C)} \quad (S3)$$

We have plotted on following figures the contrast advantage A as a function of η and T (plotted with $d = 0.0016$; $p_r = 0.0016$; $\varepsilon = 0.5$) in Fig. S1, and as a function of η and ε (plotted with $d = 0.0016$; $p_r = 0.0016$; $T = 0.0016$) in Fig. S2. One can observe that the advantage not only increases with increasing T but also when losses are added i.e. when ε decreases. Note however that adding too bright thermal light T will result in the saturation of a single photon pixel detector and therefore result in the failure of the protocol and the loss of any advantage. This technical issue can however be solved by using a detector array such as a SPAD array with a higher temporal resolution therefore reducing the likelihood of it being saturated by the thermal light.

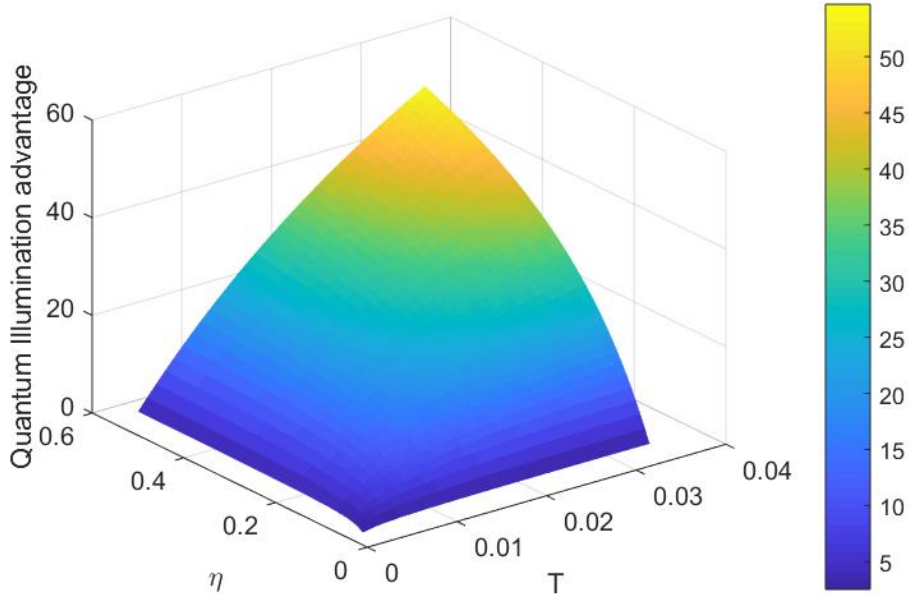


Figure S1.

The quantum illumination advantage as a function of η and T plotted with $d = 0.0016$; $p_r = 0.0016$; $\varepsilon = 0.5$.

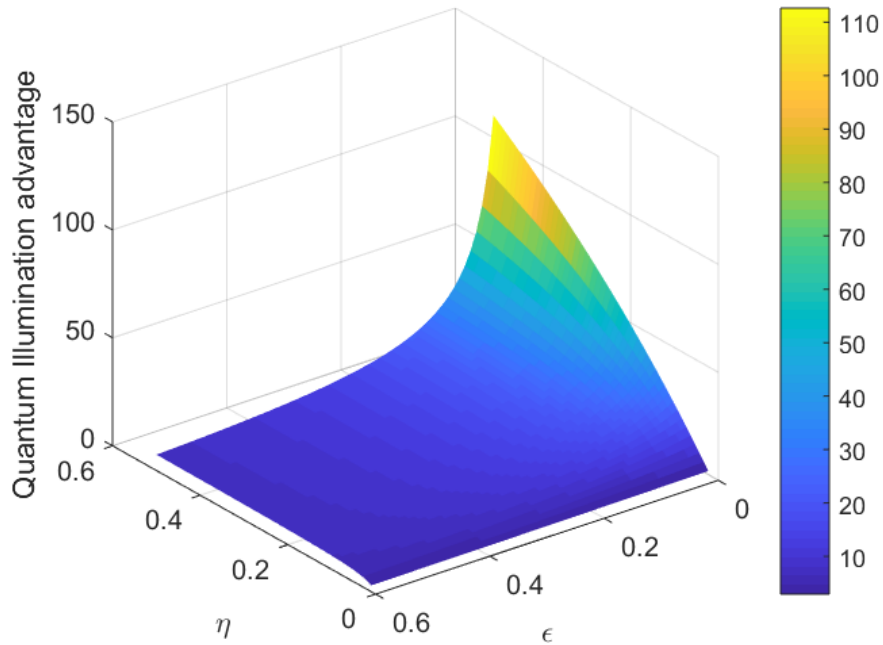
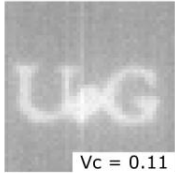
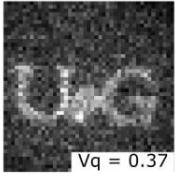
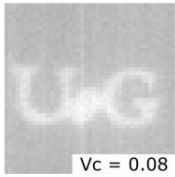
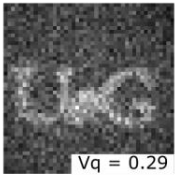
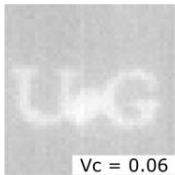
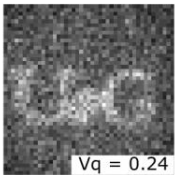
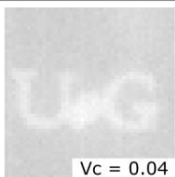
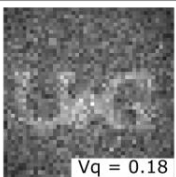
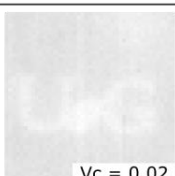
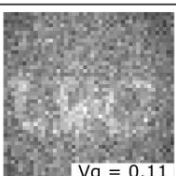
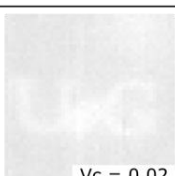
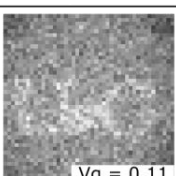
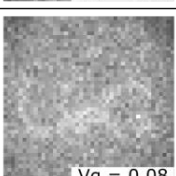
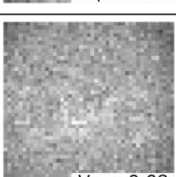


Figure S2.

The quantum illumination advantage as a function of η and ϵ (plotted with $d = 0.0016$; $p_r = 0.0016$; $T = 0.0016$).

Quantum illumination advantage in the presence of thermal noise

Figure S3 compares the results under increasing thermal light levels. It is seen that despite the introduction of increasing environmental noise events into the probe arm, the quantum illumination advantage, A , increases as the level of thermal illumination increases. This trend may also be seen in the plot of the quantum illumination advantage, A , plotted against the thermal illumination level in Fig. S4. This trend is the expected behaviour from the equations we presented in the preceding section.

Thermal background to SPDC ratio	Classically acquired image	Quantum illumination AND image	Quantum illumination advantage ratio $A = V_q/V_c$
0	 $V_c = 0.11$	 $V_q = 0.37$	3.36 ± 0.07
0.5	 $V_c = 0.08$	 $V_q = 0.29$	3.88 ± 0.10
1	 $V_c = 0.06$	 $V_q = 0.24$	4.01 ± 0.10
2	 $V_c = 0.04$	 $V_q = 0.18$	4.31 ± 0.09
4	 $V_c = 0.02$	 $V_q = 0.11$	5.18 ± 0.20
5	 $V_c = 0.02$	 $V_q = 0.11$	5.70 ± 0.21
8	 $V_c = 0.01$	 $V_q = 0.08$	6.24 ± 0.23
10	 $V_c = 0.01$	 $V_q = 0.08$	7.20 ± 0.32

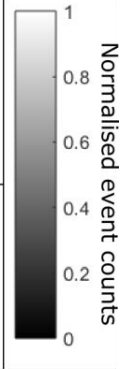


Figure S3. Imaging using quantum illumination within an increasing thermal background. Images of the UoG object with the classical image created by averaging all frames (second column), and the quantum illumination AND-image built from the sum of results of performing an AND-operation to select correlated events in the reference and probe beams (third column). The UoG object illuminated by the probe beam is imaged under the conditions of an increasing thermal background level (see the ratio of thermal illumination to SPDC illumination at 710 ± 5 nm on the left). The quantum illumination advantage A under these thermal illumination levels for images constructed over 1.5 million frames is displayed on the right. The given uncertainty is the standard error on the mean calculated using blocks of 100,000 frames. Images are 45×45 pixels.

Figure S4 shows the quantum illumination advantage A under increasing levels of thermal noise introduced into the system. Points additional to those for which results are shown in Fig. S3 are included.

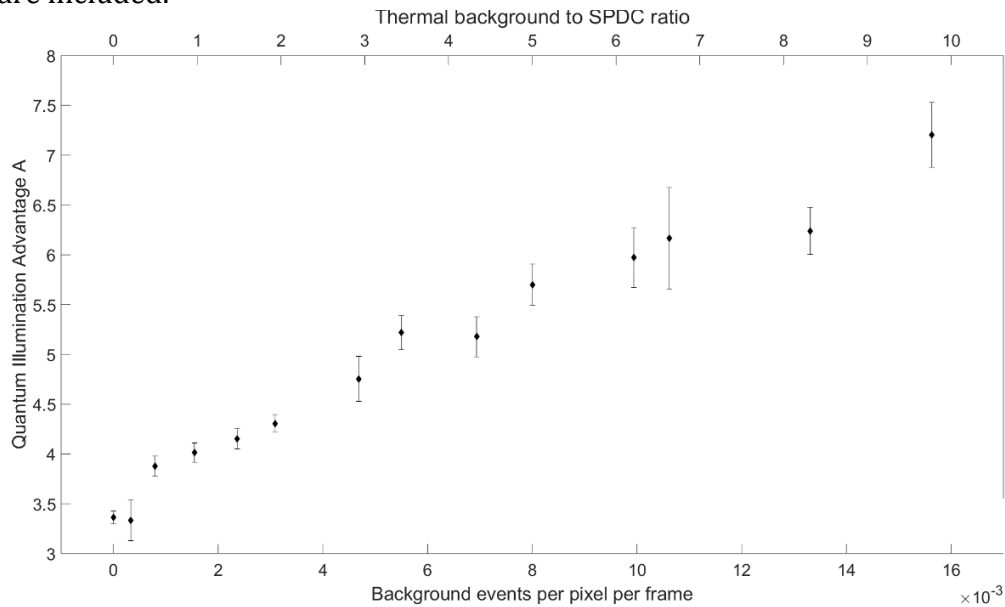


Figure S4.

Quantum illumination advantage, A , calculated over a range of increasing levels of thermal illumination. The ratio of thermal background to SPDC illumination is given for the range of levels of thermal illumination. The given uncertainty is the standard error on the mean calculated using blocks of 100,000 frames.

Quantum illumination advantage in the presence of losses

Figure S5 shows the quantum illumination advantage A under identical thermal light levels ~ 0.0016 thermal events per pixel per frame with additional optical losses introduced into the probe beam after interaction with the object. It is seen that despite the introduction of losses into the probe arm, the quantum illumination advantage, A , increases as the level of losses increases as may also be seen in Fig. 5 in the main text. This trend is the expected behaviour from the equations we presented in the preceding section.

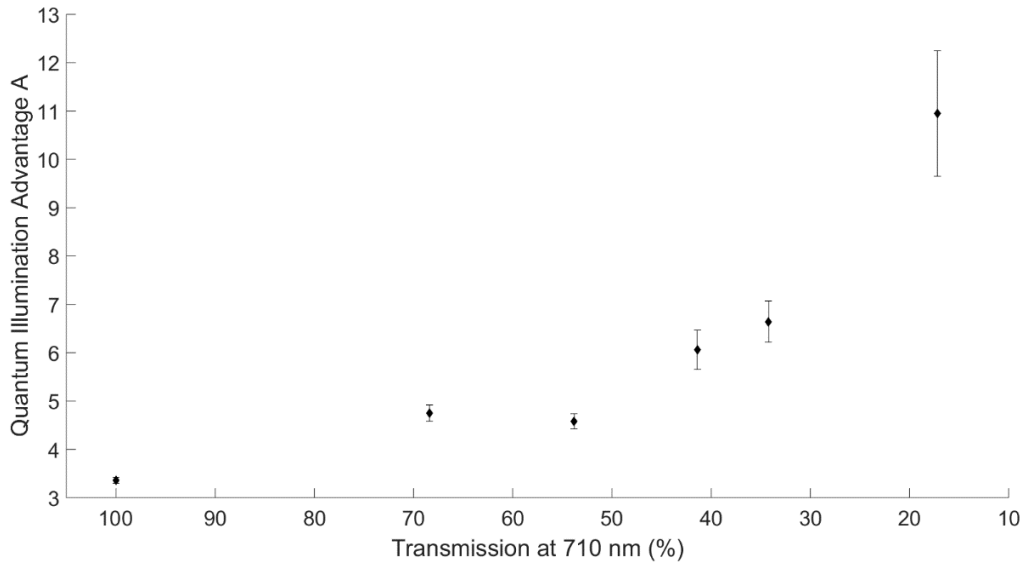


Figure S5. Plot of the quantum illumination advantage A for the system under differing levels of optical loss. The quantum illumination advantage A is assessed under these levels of optical losses for images constructed over 1.5 million frames. The given uncertainty is the standard error on the mean calculated using blocks of 100,000 frames.

Bit Error Rate determination method and analysis

In contrast to the theoretical considerations reported in (1,2), that assume the quantum illumination apparatus is ideal in that the idler arm efficiency is unity, we cannot make such an assumption. As a consequence we have to distinguish two strategies in the way one can guess the presence of a target. The first one where we do not use any knowledge about the noise or the target and for which the use of the AND-image alone will surpass a classical strategy. The second where the system is assumed to be fully calibrated and in which we know the noise levels and the transmittance of the target and for which one needs to use both the correlated AND-image data and the classical image data acquired through the quantum illumination protocol to obtain an advantage. We show here in both cases that observing a contrast advantage in the AND-images implies that one would have also an advantage in guessing the presence or absence of the target.

1) With a blind strategy

We describe here the method used to determine the bit error rate in estimating the presence or absence of a target, through both a quantum illumination and a classical illumination protocol.

The bit error rate P_{err} is determined both by the rate of predicting the presence of the target when it is absent $P_{Dark}(1)$ and the rate of prediction of its absence when it is present $P_{Bright}(0)$.

This can be written under the hypothesis of equal probability to have the target present or absent:

$$P_{err} = \frac{1}{2} P_{Dark} (1) + \frac{1}{2} P_{Bright} (0) \quad (S4)$$

To determine the error rate experimentally, one simply recognises the detection of zero events on a pixel of the image that comprises the target as revealing the absence of the target object, and the detection of one event or more as revealing the presence of the target object and try to find the optimal classical strategy in doing so (1). Knowing the ground truth (i.e. the target shape) one can assess the error rate in determining the presence or absence of the target object through this method.

In order to find the optimal classical strategy and show that the quantum strategy exhibits an advantage we make the classical prediction on an image that is composed of the sum N thresholded frames and search the value of N that minimises the classical error rate P_{err}^C for our particular experimental conditions and when no assumption of the object or the noises present can be made. In the case of quantum illumination the image is the sum of the result of the AND-operation between the reference and probe beams and therefore a signal event is added to the resulting AND-image only when a detection event occurs on the correlated idler pixel, thus post selecting the prediction. For fair comparison we use and sum the same number of post selected events in the images used for quantum illumination as were present in the sum of N thresholded frames. Which means that because the fill factor of the idler events in the detected reference beam is given by $(p + d)$ we use $\frac{N}{(p + d)}$ frames to

compose an image using the sum of post-selected events only, and make our prediction based on these images. From knowing the ground truth one can again evaluate the bit error rate.

It is important to note that because N is optimised for the classical scheme only, the quantum illumination protocol may be sub-optimal under certain conditions, nevertheless we find a systematic advantage.

Practically P_{err} is evaluated by applying a mask of the UoG target object and finding the number of background pixels that feature a detection event (false positive) and the number of pixels that comprise the UoG object but have no detected events (false negative). From our data the bit error rate across a range of thermal light levels was determined

One can predict the theoretical values of the error rate in the classical P_{err}^C and in the quantum illumination P_{err}^Q cases. Starting first with the classical case, under the hypothesis of equal probability to have the target present or absent and when one makes the prediction on an image composed by the sum of N frames one can write:

$$P_{err}^C = \frac{1}{2} (1 - (P_{Dark}^C(0))^N) + \frac{1}{2} P_{Bright}^C(0)^N \quad (S5)$$

Where $P_{Dark}^C(0) = 1 - (d + T)$ is the probability to detect no photons in a single frame when the target is absent within a particular pixel. And $P_{Bright}^C(0) = 1 - (\varepsilon p + d + T)$ is the probability to detect no photons in a single frame when the target is present within a particular pixel.

The quantum illumination strategy consists of guessing the presence or absence of the target, based on post selected detection i.e. by counting the probe events or non-events

happening at a particular pixel only when a reference event is detected on the corresponding correlated pixel. When making the prediction of presence or absence on images composed of N added such post-selected events per pixel one can write:

$$P_{err}^Q = \frac{1}{2}(1 - (P_{Dark}^Q(0))^N) + \frac{1}{2}P_{Bright}^Q(0)^N \quad (S6)$$

Where $P_{Dark}^Q(0) = 1 - (d + T)$ is the probability to detect no photons within a particular pixel of a single frame when an idler photon has been detected on the correlated pixel position and when the target is absent. And $P_{Bright}^Q(0) = \frac{p}{p+d}(1 - (\epsilon\eta + T + d)) + \frac{d}{p+d}(1 - (\epsilon p + T + d))$

is the probability to detect no photons within a particular pixel of a single frame when an idler photon has been detected on the correlated pixel position and when the target is absent.

We used these equations (S5) and (S6) to fit the experimental data reported in Fig S6.

Importantly one can note that the advantage in estimating the presence or absence of the target is based on the same mechanism as for the advantage obtained in contrast. It can be understood by realising that for equal values of accumulation of N events used in the quantum illumination and the classical case one would obtain the same background in case of the absence of the target and therefore the same error rate in wrongly predicting the absence of the target (the two first terms in equations (S5) and (S6) are equal). This means that the quantum illumination advantage in determining the presence or absence of the object in such conditions is based on a higher number of detected events in the bright parts of the images compared to the classical images. This higher rate of detected events means that the guessing the presence of the object is more accurate with quantum illumination. Therefore when the quantum and classical images have the same background, it is the higher intensity of the bright parts of the quantum image that explains the increased prediction accuracy, an increased intensity for the pixels in the frame that comprise the object with an equivalent background means also that the quantum image will exhibit a higher contrast than the classical image.

2) When the target transmittance and noises are known

Following (2) one could try to make predictions on the presence or absence of the object when the transmission of the target ϵ and the noise levels are known. In such a case the best strategy is to accumulate events and use a threshold level that minimises the error rate. This can be found theoretically by knowing the system parameters or by calibrating the system with such parameters.

In such a context and in contrast with the theoretical considerations reported in (2) that assume that the idler arm efficiency is ideal, we cannot make such an assumption. A consequence is that if in our case we simply use the AND-images to perform our estimations of the presence of the target, the results will be worse than with the classical image, because our classical image contains a greater number of events and therefore less shot noise than the quantum illumination AND-image.

However with the complete set of data acquired through quantum illumination, one can still improve the bit error rate compared to the classical case. To do so, one needs to use a combination of both the classical data (classical images) and the non-classical data (the

AND-images) in a similar way that the optimal strategy for sub-shot noise measurement is to use both correlated and uncorrelated data (20). To understand that one can observe a quantum illumination advantage means that the ensemble of post selected events detected within the quantum illumination AND-image image are more valuable than the same number of non-correlated events in predicting the presence of the object. Indeed for an equal number of events the noise in both the bright parts and the dark parts of the image will be the same in both the AND-image and a classical image, however the contrast is higher in the AND-image than classical image with the same number of events. This is because a higher contrast means that the places where the object is present and absent are further apart in intensities, and therefore for same shot noise level the optimal guess will be more accurate in the AND-image. However because of the non-ideal idler arm efficiency η one will have more events in the total classical image than in the AND-image. The best strategy then is to use a combination of both images in order to give more weight to the correlated events than to the uncorrelated ones. And as long as the AND-image exhibits a contrast advantage, this will lead to an improvement of the bit error rate over the simple use of the classically acquired image.

Practically this means that one would have to use an optimal image:

$$I_{Opt} = (1 - s)I_{Average} + sI_{AND} \quad (S7)$$

Where the weight s ($0 \leq s \leq 1$) is in particular dependent on the value of η , the greater the efficiency η the more events I_{AND} are kept and the greater s should be, $s = 1$ if $\eta = 1$. It also depends on any other parameters affecting the contrast advantage. The higher the contrast advantage, the more useful I_{AND} will be and therefore the greater s should be. In particular a greater timing resolution in the detection of the correlations can further reduce the probability of detecting false coincidences due to the thermal light at a given light level. This means that a better timing resolution such as accessible with SPAD array can improve the contrast advantage and will therefore mean that the value used for s in such circumstances should be greater. Finally, we would like to conclude this paragraph by remarking again that a contrast advantage in I_{AND} implies that it can be used to build a strategy that is better than the classical strategy, which means that a contrast advantage through quantum illumination implies an error rate advantage.

Bit error Rate Results

Here we present an analysis of how this protocol may be used in an application where the presence or absence of an object needs to be assessed. This is the context in which Lloyd (1) originally proposed the quantum illumination protocol and in which it has clear applications in realising quantum LIDAR or quantum radar applications. The error rate in detecting the presence or absence of an object in the probe beam path is assessed over a range of light levels using the 'blind' strategy in which no prior information is assumed in Fig. S6. The advantage in the probability of successfully determining the presence or

absence of an object for quantum illumination may be seen over the range of thermal light levels. The points lie below the curve for the quantum illumination AND-image due to the thermal illumination not being entirely flat as may be seen in the images presented in Fig. S3.

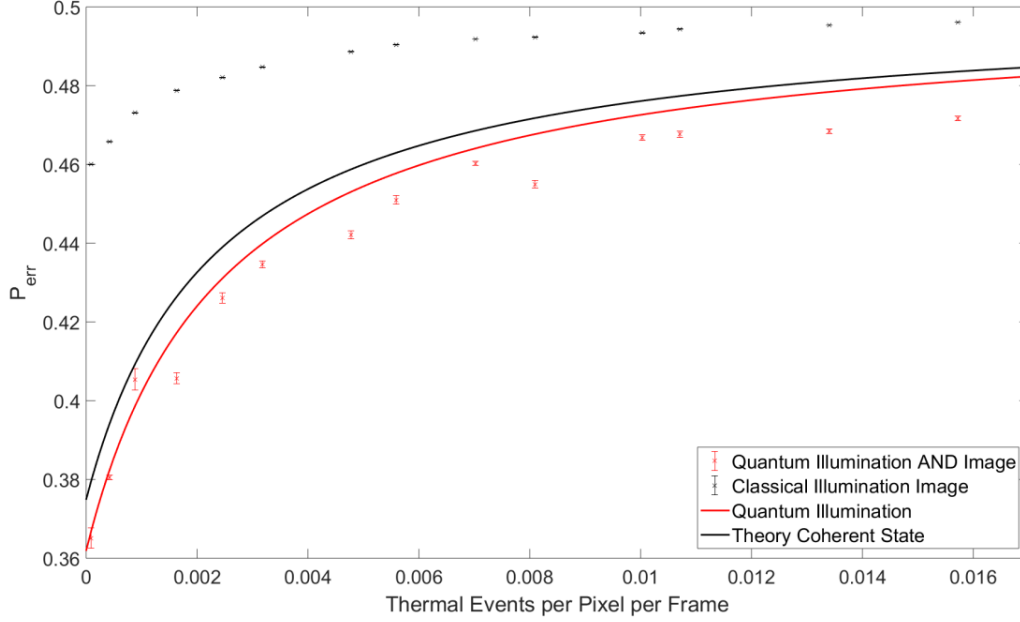


Figure S6. The bit error rate P_{err} of detecting a target calculated over a range of thermal light levels. The classical data is represented by the black crosses and the quantum illumination AND-image by the red crosses. The curve in black represents the theoretical optimum bit error rate for an image constructed from coherent state illumination. The red curve represents the equivalent curve for the quantum illumination AND-image calculated using experimental parameters. These theoretical curves are valid under the assumption of an unknown background and target object and assuming Poissonian camera dark noise and thermal light. Error bars are the standard error on the mean for the bit error rate.

In the case of the second strategy a weighted sum (see equation S7) of the classical image and the quantum illumination AND-image is used to calculate the bit error rate. For both the classical image and also the weighted sum of the classical and AND-image the mean and standard deviation of both the background pixels (μ_{bg} and σ_{bg}) and also of the pixels that comprise the UoG object (μ_{UoG} and σ_{UoG}) are found. The threshold T is then set such that:

$$T = \mu_{UoG} - n_{sd}\sigma_{UoG} = \mu_{bg} - n_{sd}\sigma_{bg} \quad (S8)$$

where:

$$n_{sd} = \frac{\mu_{UoG} - \mu_{bg}}{\sigma_{UoG} + \sigma_{bg}} \quad (S9)$$

The images are then thresholded appropriately and the bit error rate calculated. This is performed over a range of weights s ($0 \leq s \leq 1$) and the minimum value for the bit error rate determined.

It may be seen in Fig. S7 that the advantage in the bit error rate is decreased compared to that in the 'blind' strategy. This is due to non-ideal idler arm efficiency resulting in a non-unity value for the weight value s .

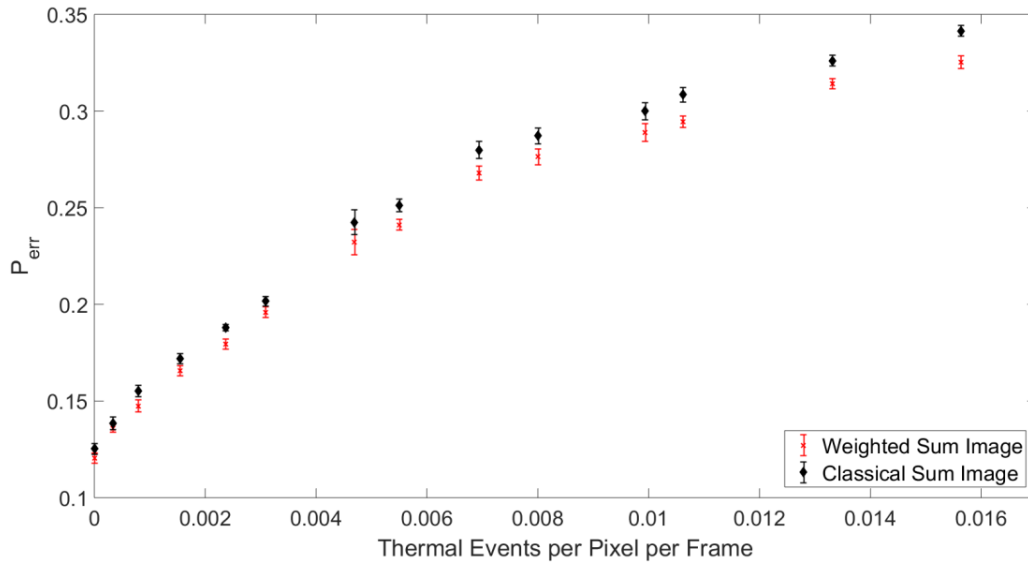


Figure S7. The bit error rate P_{err} of detecting a target calculated over a range of thermal light levels using the second method. The purely classical data is represented by the black crosses and the weighted sum of the classical image and the quantum illumination AND-image by the red crosses. The given uncertainty is the standard error on the mean calculated using blocks of 100,000 frames.

The values of s calculated to optimise bit error rate of the compound images as per method 2 of the bit error rate calculation for the UoG objects under a range of differing thermal illumination conditions are shown in Table S1 accompanying Figure S7. The average value of s for this set of data is 0.7702 ± 0.0401 , and the optimal values found for each light level seems consistent (within the error bars). The fact that these values for s are non-unity indicates that a greater advantage may be achieved should the system efficiency be further increased, but also with a better correlation timing resolutions that could lead to an improved contrast advantage.

Background events per pixel per frame ($\times 10^{-4}$)	s weight value
0	0.6542 ± 0.0544
4	0.7642 ± 0.0687
8	0.7678 ± 0.0255

16	0.7457 +/- 0.0419
24	0.7785 +/- 0.0110
32	0.6610 +/- 0.0638
48	0.8389 +/- 0.0096
55	0.7481 +/- 0.0570
70	0.8118 +/- 0.0180
80	0.8160 +/- 0.0204
100	0.8021 +/- 0.0284
104	0.7991 +/- 0.0066
128	0.8166 +/- 0.0215
160	0.7789 +/- 0.0536

Table S1. Table of the average s weight values calculated over a range of thermal light levels using the second method for each of the different levels of thermal illumination. The given uncertainty is the standard error on the mean calculated using blocks of 100,000 frames.